THE ASTROPHYSICAL JOURNAL, 538:203–216, 2000 July 20

NONTHERMAL EMISSION FROM A SUPERNOVA REMNANT IN A MOLECULAR CLOUD

A. M. BYKOV
A. F. Ioffe Institute for Physics and Technology, St. Petersburg, 194021, Russia
R. A. CHEVALIER
Department of Astronomy, University of Virginia, P.O. Box 3818, Charlottesville, VA 22903
D. C. ELLISON
Physics Department, North Carolina State University, Raleigh, NC 27695
AND
YU. A. UVAROV
A. F. Ioffe Institute for Physics and Technology, St. Petersburg, 194021, Russia
Received 1999 September 3; accepted 2000 March 1

ABSTRACT

In evolved supernova remnants (SNRs) interacting with molecular clouds, a highly inhomogeneous structure consisting of a forward shock of moderate Mach number, a cooling layer, a dense radiative shell, and an interior region filled with hot tenuous plasma is expected. We present a model of nonthermal electron injection, acceleration, and propagation in that environment and find that these SNRs are efficient electron accelerators and sources of hard X-ray and γ-ray emission. A forward shock of velocity $v_s \gtrsim 100$ km s^{-1} with an ionized precursor propagating into the molecular cloud accompanied by magnetohydrodynamic turbulence provides a spatially inhomogeneous distribution of nonthermal electrons. The energy spectrum of the nonthermal electrons is shaped by the joint action of first- and second-order Fermi acceleration in a turbulent plasma with substantial Coulomb losses. Bremsstrahlung, synchrotron, and inverse Compton radiation of the nonthermal electrons produce multiwavelength photon spectra in quantitative agreement with the radio and hard emission from IC 443 observed by *ASCA* and EGRET. We distinguish interclump shock wave emission from molecular clump shock wave emission; particles reach higher energies in the interclump shock, and that is the likely source of γ-ray emission and radio synchrotron emission. Spatially resolved X-ray and γ-ray spectra from the SNRs IC 443, W44, and 3C 391 as might be observed with *BeppoSAX*, *Chandra XRO*, *XMM*, *International Gamma-Ray Astrophysical Laboratory*, and *Gamma-Ray Large Area Space Telescope* would distinguish the contribution of the energetic lepton component to the γ-rays observed by EGRET, constraining the cosmic-ray nuclear component spectra in these SNRs. These data would provide a valuable tool for studying the complex structure of molecular clouds where SNR radiative shocks interact with dense molecular clumps.

Subject headings: acceleration of particles — cosmic rays — radiation mechanisms: nonthermal — supernova remnants

1. INTRODUCTION

Supernovae and their remnants have long been identified as likely sites of Galactic cosmic-ray acceleration. Evidence for electron acceleration first came from observations of radio synchrotron radiation. The observation of nonthermal X-ray emission from SN 1006 by *ASCA* has provided evidence for electron acceleration up to ~ 100 TeV (Koyama et al. 1995; Reynolds 1998). The proton cosmic-ray component is more difficult to observe, but it has long been recognized that pion decays from collisions with interstellar gas could give an observable flux of 0.1–1 GeV photons. Initial estimates of γ-ray emission from supernova remnants (SNRs), concentrating on the component resulting from pion decays, were made by Chevalier (1977), Blandford & Cowie (1982), and Drury, Aharonian, & Völk (1994). When γ-ray emission was apparently detected from SNRs by the *Compton Gamma Ray Observatory* (*CGRO*), the γ-ray spectrum could not be fitted by a pure pion decay spectrum and some other component was needed (Esposito et al. 1996; Sturner et al. 1997; Gaisser, Protheroe, & Stanev 1998). In addition to the pion decays, the relevant processes are bremsstrahlung emission of relativistic electrons and inverse Compton emission. Gaisser et al. (1998) modeled these processes in detail in order to fit the observed γ-ray spectra of the remnants IC 443 and γ Cygni. They assumed acceleration to a power-law spectrum in the shock front and determined the spectral index, electron-to-proton ratio, and the upper energy cutoff.

The evolution of the relativistic component in an SNR has been modeled by a number of groups. Sturner et al. (1997) assumed particle acceleration in the shock front with an E^{-2} energy spectrum and followed the evolution of the particle spectrum. Their SNR model was homogeneous: a factor 4 density jump at the shock front, constant density in the interior, and a constant magnetic field in the interior. Their shock acceleration model had a diffusion length parameter that was important for the maximum energy reached by the particles. They modeled the nonthermal emission from IC 443 as synchrotron emission in the radio and bremsstrahlung in γ-rays. De Jager & Mastichiadis (1997) dealt with the same processes in W44 as well as inverse Compton emission. They noted that the observed radio spectrum is flatter than would be expected from shock acceleration of newly injected particles and suggested that

the particles originated from a pulsar in the SNR. Recently, Ostrowski (1999) showed that second-order electron acceleration by the turbulent medium just after the shock could flatten the spectra to account for the radio observations of IC 443. Baring et al. (1999) presented calculations of the broadband emission from nonlinear shock models of shell-type SNRs. They used Sedov adiabatic shock dynamics in a homogeneous medium and a Monte Carlo simulation of the particle acceleration taking into account the nonlinear shock structure. The set of models considered by Baring et al. (1999) covers the range of shock speeds 490 km $s^{-1} \leq v_S \leq 4000$ km s^{-1} and ambient medium number densities 10^{-3} $cm^{-3} \leq n \leq 1$ cm^{-3}.

Massive stars that are the likely progenitors of core collapse supernovae are expected to be spatially correlated with molecular clouds. The remnants that are likely to be γ-ray sources in *CGRO* observations (Esposito et al. 1996) also show evidence for interaction with molecular gas. Chevalier (1999) recently studied the evolution of SNRs in molecular clouds and concluded that many aspects of the multiwavelength observations could be understood in a model where the remnants evolve in the interclump medium of a molecular cloud, which has density of 5–25 H atoms cm^{-3}, and become radiative at radii ~ 6 pc. The compression in the radiative shell is limited by the magnetic field. Molecular emission occurs when the radiative shell collides with molecular clumps. IC 443 is the remnant with the best evidence for high-energy emission and also shows clear evidence for interaction of the shock with a molecular cloud (e.g., Burton et al. 1990; van Dishoeck et al. 1993; Cesarsky et al. 1999).

Most of the current models of particle acceleration in SNRs have dealt with adiabatic remnants in a homogeneous medium (see, however, the model of Boulares & Cox 1988 for the Cygnus Loop and the model of Jones & Kang 1993). In contrast, our aims here are to examine in detail the nonthermal emission of radiative SNRs in molecular clouds using a kinetic model of electron injection, acceleration, and propagation, including the inhomogeneous structure deduced from multiwavelength SNR observations. We use global MHD (magnetohydrodynamic) models of SNRs interacting with molecular clouds as described by Chevalier (1999), including the theory of radiative shock structure by Shull & McKee (1979) and the kinetic model of electron injection and acceleration by shocks from Bykov & Uvarov (1999). The model described here is relevant to the mixed-morphology SNRs (Rho & Petre 1998) if they are interacting with molecular clouds. These remnants comprise a sizable fraction of the Galactic SNR population.

The plan of our paper is as follows. In § 2, we treat the energy spectrum of energetic electrons as they pass through the regions associated with a radiative shock wave. We include the shock acceleration of particles from the thermal pool. In § 3, we present calculations of the nonthermal emission from the relativistic particles, including emission from shocks in clumps as well as emission from the radiative shock wave in the interclump region. Our model is specifically applied to the well-observed remnant IC 443, although we expect it to more generally apply to other SNRs in molecular clouds. We also examine the ionization by energetic particles and the energy involved in the relativistic particles. A discussion of results and future prospects is in § 4. A detailed discussion of expected range of densities, shock velocities, and magnetic fields determined from multiwavelength observations of IC 443, W44, and 3C 391 was given in the paper by Chevalier (1999 and references therein).

2. EVOLUTION OF NONTHERMAL ELECTRONS

The structure of the flow expected in a radiative shock can be divided into the following regions (see, e.g., Draine & McKee 1993): (I) a region of preshock gas ionized and heated by UV (ultraviolet) emission and fast particles from the shock; (II) a shock transition region; (III) a postshock cooling layer; (IV) a cold shell of swept-up gas; and (V) a region of hot low-density gas interior to the shock. Radiative shocks are subject to thermal instabilities (Chevalier & Imamura 1982; Bertschinger 1986) as well as dynamical instabilities (Vishniac 1983; Blondin et al. 1998). Although the effect of inhomogeneous magnetic fields on the stability of radiative shock flow is yet to be studied, MHD turbulence is expected in such a system. The transport and acceleration of nonthermal particles in the violent SNR environment are governed by the MHD flow and depend on the ionization structure and on the spectrum of MHD turbulence. Shocks with velocity $v_{S7} \geq 1.1$ generate sufficient UV radiation for full preionization of hydrogen and helium (He^+) in the preshock region, where the gas temperature is typically $\sim 10^4$ K (Shull & McKee 1979). Here v_{S7} is the shock velocity measured in units of 100 km s^{-1} and n_1 is the ion number density measured in units of 10 cm^{-3}. Shocks with $v_{S7} \sim 1.5$ propagating in a medium with $n_1 \sim 1$ photoionize gas ahead of the viscous jump to a depth $N_i \gtrsim 3 \times 10^{17}$ cm^{-2}. The shock transition in such a case is collisionless and supercritical unless the preshock magnetic field is above $\sim 4 \times 10^{-5} n_1^{0.5}$ G.

The geometry of the magnetic field is important for the efficiency of electron injection and acceleration. It has been argued (e.g., Levinson 1996; McClements et al. 1997) that quasi-perpendicular shocks are an efficient source of freshly injected electrons if their speed $v_s \geq (m_e/m_p)^{0.5} c$; the injection efficiency drops sharply below that threshold. On the other hand, Bykov & Uvarov (1999) have shown that quasi-parallel MHD shocks of moderate Alfvén Mach number $M_A \leq (m_e/m_p)^{-0.5}$ are suitable sites of electron injection and acceleration. The SNR shock waves in molecular clouds are expected to be in this regime of Mach number. Thus, we shall discuss below the quasi-parallel portion of the shock (magnetic field inclinations $\leq \pi/4$) propagating into a molecular cloud with $v_{S7} \sim 1.5$.

Nonresonant interactions of the electrons with fluctuations, generated by kinetic instabilities of the ions in the transition region of a quasi-parallel supercritical shock, play the main role in heating and preacceleration of the electrons. The electron heating and preacceleration (injection) occur in the collisionless shock front transition region on a scale Δ of several hundred inertial lengths of the ions, l_i (Bykov & Uvarov 1999). Here $l_i = c/\omega_{pi} \sim 9 \times 10^6 n_1^{-0.5}$ cm and ω_{pi} is the ion plasma frequency. For an SNR shock in a molecular cloud, the scale $\Delta \sim 10^9$ cm is much shorter than the scales of all the other regions.

To accelerate electrons injected in the shock transition region to relativistic energy $E(p)$, MHD turbulence should fill the acceleration region, which has a scale $l_a \sim k_m(p)/v_s$. Here $k_m = \max(k_i)$, where $k_i(p)$ is the diffusion coefficient of an electron of momentum p and $i = (\mathrm{I}), (\mathrm{III})$ refers to the regions defined above. To provide the conditions for efficient transformation of the MHD flow power to the acceler-

ated electrons, the MHD turbulent fluctuation spectrum in the vicinity of the shock should extend to scales $l \geq r_e(p)$ (resonant scattering), where $r_e(p)$ is the gyroradius of an electron with momentum p. The MHD fluctuations responsible for the electron scattering are collisionless for particles with energies up to a GeV because the ion-neutral collision length is above 10^{14} cm for typical parameters of the radiative shock described below [a keV electron has $r_e \approx 10^8 (B/10^{-6}\ \mathrm{G})^{-1}$ cm].

To calculate the spectra of nonthermal electrons in the regions i = (I)–(IV), we use a kinetic equation for the nearly isotropic distribution function $N_i(z, p, t)$:

$$\frac{\partial}{\partial t} N_i + u_i(z) \frac{\partial}{\partial z} N_i - \frac{p}{3} \frac{\partial}{\partial p} N_i \left(\frac{\partial}{\partial z} u_i \right) = k_i(p) \frac{\partial^2 N_i(z, p)}{\partial z^2} + \frac{1}{p^2} \frac{\partial}{\partial p} p^2 D_i(p) \frac{\partial N_i}{\partial p} + \frac{1}{p^2} \frac{\partial}{\partial p} [p^2 L_i(p) N_i] . \quad (1)$$

The Fokker-Planck–type equation (1) takes into account diffusion and advection [with bulk velocity $u_i(z)$] of an electron in phase space due to particle interaction with MHD waves and the large-scale MHD flow (Bykov & Toptygin 1993). Here $L_i(p)$ is the momentum loss rate of an electron due to Coulomb collisions in a partially ionized plasma (e.g., Ginzburg 1979). The momentum diffusion coefficient $D(p)$ is responsible for second-order Fermi acceleration, and $k_i(p)$ is the fast particle spatial diffusion coefficient. For low-energy electrons (i.e., $E \leq E_C$), Coulomb and ionization losses are important in the regions (I)–(V), except for the narrow shock transition region (II) where acceleration is fast enough to overcome losses and nonthermal electron injection occurs. The characteristic energy E_C depends on the plasma density and ionization state, magnetic field, and fast particle diffusion coefficients $k_i(p)$ and $D_{(I)}(p)$. The corresponding momentum p_{ci} can be estimated as the point where the last two terms in equation (1) are equal. We used the energy E_C calculated simultaneously with the electron distribution function as a convenient parameter to distinguish between different possible models of MHD turbulence in the postshock cooling layer of the radiative shock structure (see below in this section).

The diffusion coefficients $k_{(I)}(p)$ and $D_{(I)}(p)$ depend on the spectrum of the collisionless MHD turbulence, which is poorly understood. A plausible approximation for the diffusion coefficients $k_i(p)$ was assumed here. For all of the regions we used the following parameterization:

$$k_i(p) = k_{i0} \begin{cases} 1 , & p_T \leq p \leq p_* \\ v p^a / v_* p_*^a , & p_* \leq p \leq p_{**} \\ c p^2 / (p_{**}^{2-a} p_*^a v_*) , & p_{**} \leq p \leq p_m . \end{cases} \quad (2)$$

Here p_T is the momentum of the upstream thermal electrons, p_m is the momentum corresponding to the upper cutoff energy E_m (see eq. [3]), and p_* and p_{**} are defined in the next paragraph. The standard relation for the momentum diffusion coefficient $D_i(p) = p^2 w_i^2 / 9 k_i(p)$ (e.g., Berezinsky et al. 1990) was used. In the low-energy regime $p \leq p_*$, the particle transport is dominated by large-scale turbulent advection (Bykov & Toptygin 1993). The large-scale turbulence is due to stochastic MHD plasma motions on scales Λ longer than the particle mean free path due to resonant scatterings. The sources of MHD turbulent motions are the shock wave instabilities mentioned at the beginning of this section. The large-scale vortex rms velocity w_i typically is a fraction of bulk speed u_i. The spatial diffusion is energy independent below p_* and $k_{i0} \sim w_i \Lambda$. For $p_* \leq p \leq p_{**}$, electrons are scattered by resonant MHD waves presumably generated by the streaming instability of shock-accelerated particles (e.g., Blandford & Eichler 1987; Jones & Ellison 1991). In this case, w_i is close to the Alfvén velocity v_A and $k_i(p)$ is the electron diffusion coefficient due to resonant wave-particle interactions. If the power spectrum of magnetic field fluctuations of Alfvénic turbulence for the resonant fluctuations is approximated as $dB_k^2/dk \sim k^{-\theta}$, then the power-law index a (eq. [2]) is related to the index θ as $a = 2 - \theta$. An important particular case corresponding to $a = 1$ can be written as $k_i(p) = \frac{1}{3} \eta_i v r_e(p)$. The parameter η_i determines the scattering "strength," and strong scattering (Bohm limit) corresponds to $\eta_i \sim 1$. The diffusion model with $a = 1$ was successfully used for modeling the observed anomalous cosmic-ray proton fluxes in the interplanetary medium (Ellison, Jones, & Baring 1999) and in the Monte Carlo simulations of nonlinear shocks in the shell-type SNRs (e.g., Baring et al. 1999). The momentum p_* in our model can be estimated from the equation $\frac{1}{3} \eta_i v r_e(p_*) = w_i \Lambda$.

MHD waves in the partially ionized plasma of the radiative shock flow are subject to ion-neutral damping (e.g., Völk, Morfill, & Forman 1981). We define the momentum p_{**} from the condition $r_e(p_{**}) = \lambda_{\mathrm{in}}$, where λ_{in} is determined from the relation $\lambda_{\mathrm{in}} = 2\pi v_A / \Gamma_{\mathrm{in}}$ and Γ_{in} is the Alfvén wave damping rate due to ion-neutral collisions (Kulsrud & Cesarsky 1971). For $p \geq p_{**}$, electrons are scattered by nonresonant small-scale waves.

The limits imposed on the diffusive shock acceleration of particles due to ion-neutral MHD wave damping have been discussed by Draine & McKee (1993) and Drury, Duffy, & Kirk (1996). They considered the spectra of Alfvén waves driven by the instabilities of shock-accelerated ions in a partially ionized plasma. Drury et al. (1996) obtained the upper cutoff energy of a proton due to ion-neutral wave damping

$$E_m \leq v_{S7}^3 T_4^{-0.4} n_n^{-1} n_i^{0.5} \mathscr{P}_{-1}^{CR} \ \mathrm{GeV} , \quad (3)$$

where n_n is the neutral particle density, n_i is the ion density (both are measured in cm^{-3}), and $\mathscr{P}_{-1}^{CR}$ is the total particle pressure normalized to 10% of the shock ram pressure. The ionization structure of the preshock region is inhomogeneous, so the ion number density, temperature, and other numbers in equation (3) must be taken at an upstream distance $\sim k_{(I)}(E_m)/v_S$ from the collisionless shock transition. Application to our model yields $E_m \sim 10$ GeV if $v_{S7} \sim$ 1.1–1.5 and $k_{(I)}(E_m) \sim 10^{24}\ \mathrm{cm}^2\ \mathrm{s}^{-1}$ because of the high ionization in the preshock region (I) and the postshock cooling layer (region [III]) provided by the UV radiation. One can justify the same value of E_m for the electrons because the synchrotron and inverse Compton losses are relatively unimportant for $E_m \sim 10$ GeV.

Region (I).—In the preshock region of the shock with $v_{S7} \gtrsim 1.1$, we assume a highly ionized plasma of temperature $T_4 \sim 1$ up to depths similar to a few times 10^{17} cm^{-2} upstream. For the IC 443 preshock region, we adopted a density $\sim 25\ \mathrm{cm}^{-3}$ and $v_{S7} \approx 1.5$ (Fesen & Kirshner 1980). The magnetic field $B_{\parallel} \approx 10^{-5}$ G (Chevalier

1999), while $B_\perp \approx 5 \times 10^{-6}$ G (the inclination is assumed to be $\sim \pi/6$). The Alfvén velocity here is about 5 km s^{-1}. We assume a conservative diffusion model in the shock upstream region where $k_{(I)}(p)$ has $a = 1$ and the moderate scattering "strength" $10 \leq \eta_{(I)} \leq 100$ (Ellison et al. 1999).

Region (II).—In the shock transition region, injection and heating of the electrons occur as a result of nonresonant interactions with strong MHD fluctuations generated by the ions. Following the model developed by Bykov & Uvarov (1999), we take

$$D_{(II)}(p) \approx p^2 \bar{C} \left(\frac{\delta B}{B_0}\right)^2 \left(\frac{v_A}{v}\right)^2 \left(\frac{v}{l_i}\right), \quad (4)$$

where $\bar{C} \sim 1$ and $\delta B \gtrsim B_0$. The Alfvénic Mach number of the shock, $M_A \gtrsim 10$, is moderate for our situation. Nevertheless, the effect of the accelerated particle pressure on the shock structure could be important (see, e.g., Jones & Ellison 1991; Baring et al. 1999). An exact treatment of the effect is not feasible in our model because it would require a kinetic description of the ion injection. We accounted for the effect by correction of the total shock compression ratio δ_t and by introducing an extended modified shock structure with a precursor and a subshock with compression ratio $\delta_s \lesssim \delta_t$ (e.g., Jones & Ellison 1991). In our case with Mach numbers $M \gtrsim 15$, the estimated extra compression was about 10%, and thus $\delta_t \approx 4.4$. A subshock compression ratio $\delta_s \approx 3.3$ is consistent with the assumption of substantial heating of the precursor gas due to wave dissipation (Berezhko & Ellison 1999). These numbers are in agreement with those from a hybrid simulation of nonlinear shock structure (Giacalone et al. 1997). We found that the resulting high-energy emission spectra are sensitive to the particular choice of precursor flow structure in the MeV regime. The keV and GeV emission is not sensitive to the structure if the compression ratios δ_t and δ_s are fixed.

Region (III).—The postshock cooling layer has a column density $\sim 3 \times 10^{17}$ cm^{-2} of highly ionized plasma with an initial density about δ_t times that of the preshock one. The Alfvén velocity in the highly ionized portion of region (III) is similar to that at the preshock region, ~ 5 km s^{-1}. Large-scale vorticity with an amplitude $\lesssim 20$ km s^{-1} on scales $\Lambda \lesssim 10^{14}$ cm may occur here because of shell instabilities of the radiative shock with $v_{S7} \sim 1.5$ (see, e.g., § 5 in the review by Draine & McKee 1993). This would dominate the low-energy electron propagation, providing a spatial diffusion coefficient of $\sim 10^{20}$ cm^2 s^{-1} for the radiative shock parameters described above.

Coulomb losses are important here for electrons with energies below $E_C \approx 20$ keV if the large-scale turbulent velocity has a substantial longitudinal component with $w_{(III)} \approx 20$ m s^{-1}; $E_C \gtrsim 8$ MeV is expected in the absence of a longitudinal component of large-scale turbulence in the postshock cooling layer because the Coulomb losses are overcome by resonant interaction with Alfvén waves. Since the Alfvén velocity is relatively low (~ 5 km s^{-1}), the value of E_C is much higher in that case. An accurate description of MHD turbulence in the postshock cooling layer is not available now. Thus, we considered both limiting cases described above and show the uncertainty introduced by the lack of data concerning the large-scale turbulence properties in Figure 1. To avoid overestimating the nonthermal emission, we used a conservative minimum value of $E_C = 120$ keV for the radiative shock structure described above, although one could expect $E_C \sim 20$ keV in the most favorable case.

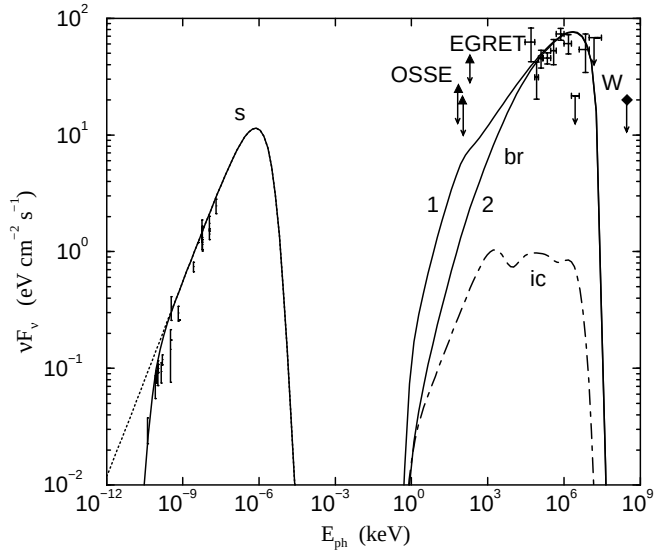

FIG. 1.—Broadband νF_ν spectrum of the shell of IC 443 (distance 1.5 kpc) calculated from a model of nonthermal electron production by a radiative shock with direct injection of electrons from the thermal pool. The shock velocity is 150 km s^{-1}, the interclump number density is 25 cm^{-3}, and the interclump magnetic field is 1.1×10^{-5} G. The electron diffusion coefficient (see eq. [2]) is $k_{(III)0} = 1.1 \times 10^{20}$ cm^{-2} s^{-1}, $a = 1.0$, $E(p_*) = 1$ MeV, and $E(p_{**}) = 20$ GeV (eq. [3]). The radiative shell parameters are described in § 2. The two solid curves labeled 1 and 2 correspond to two limiting values of E_C: $E_C = 120$ keV (*curve 1*) and $E_C = 2$ GeV (*curve 2*). Interstellar absorption of the radio spectrum is treated as described in the text. The extended inverse Compton emission from the whole remnant is shown as a dashed line. The observational data points are from Esposito et al. (1996) for the EGRET source 2EG J0618+2234 and Erickson & Mahoney (1985) for the IC 443 radio spectrum. Upper limits for MeV emission are from *OSSE* observations (Sturner et al. 1997). Upper limits for γ-rays ≥ 300 GeV are from Whipple observations of IC 443 (Buckley et al. 1998).

Region (IV).—The density and temperature in the radiative shell depend on the preshock density, magnetic field, and abundances (Shull & McKee 1979; Chevalier 1999). From the model of Chevalier (1999) for the above preshock parameters, we adopted $n \approx 275$ cm^{-3} ($N_H \approx 1.6 \times 10^{20}$ cm^{-2}) and $T \sim 10^2$ K in the dense radiative shell. The mass of the dense radiative shell is $\sim 1000\ M_\odot$ and its magnetic field is $\sim 6 \times 10^{-5}$ G. The ionization in the dense radiative shell is supported at the level of about a percent by shock-accelerated particles penetrating into the shell (see § 3.5 for details). The phase velocity of the high-frequency collisionless Alfvén waves which are responsible for electron resonant scattering is about 50 km s^{-1}; it is determined by the number density of the ions. The Coulomb loss rate of the electrons is then dominated by the neutral component.

We numerically calculated the electron distribution function in regions (I)–(IV). The results were then used in calculations of the nonthermal emission.

3. NONTHERMAL EMISSION FROM IC 443

The SNR IC 443 (G189.1+3.0) is a very good candidate for testing our model, because the interaction of the SNR with a molecular cloud was established from radio and infrared line observations (e.g., DeNoyer 1979; Mufson et al. 1986; Burton et al. 1990; van Dishoeck et al. 1993;

Richter, Graham, & Wright 1995; Claussen et al. 1997). The high-energy fluxes are somewhat better determined than in other cases. Although we concentrate on IC 443, we briefly mention the case of W44, where observations of OH masers and CO clumps again provide convincing evidence of molecular cloud interaction (Claussen et al. 1997; Frail & Mitchell 1998).

To model the nonthermal emission from the shell of IC 443, we integrated the local emissivities over the radiative shock structure (regions [I]–[IV]). As a parcel of gas containing accelerated nonthermal electrons evolves through the radiative shock structure including the dense shell, the local emissivity from bremsstrahlung and inverse Compton was calculated using standard theory (see Appendix A for details). The electron-ion bremsstrahlung emission differential cross sections (Bethe-Heitler formulae) were taken from Akhiezer & Berestetsky (1957) taking into account the Elwert factor, which is important for modeling the keV emission. The electron-electron bremsstrahlung contribution to the γ-ray emissivity was calculated using cross sections derived by Haug (1975). For the inverse Compton emissivity of IC 443, we used the same description of the background photon field as Gaisser et al. (1998). The hard emission production cross sections used in our calculations are similar to those used recently by other authors (Asvarov et al. 1990; Sturner et al. 1997; Gaisser et al. 1998; Baring et al. 1999). We also estimated the contribution of pion decays to the γ-ray emission using a model for the proton component and the cross sections from Dermer (1986). The resulting emission in the EGRET regime was roughly 7 times below that from electron bremsstrahlung, which is consistent with the results of Sturner et al. (1997). We do not discuss the pion component further.

The synchrotron emission of the electrons calculated using the scheme described by Ginzburg (1979) can be compared to the radio observations and to the upper limits at higher frequencies. We also included free-free absorption of low-frequency radio waves (Fig. 1, *dotted line*). The synchrotron losses of a relativistic electron were included following Ginzburg (1979); bremsstrahlung energy losses are relatively unimportant in our case.

3.1. *Energetic Nonthermal Emission from the Shell*

The emission was integrated over the regions of the radiative shock in order to model the spectrum of the entire shell. Region (IV) is the dominant contributor to the synchrotron and bremsstrahlung emission. The results in Figure 1 can be compared to the *ASCA* and EGRET observations of SNRs, as well as to the significant upper limits that have been set at TeV energies by Whipple observations (Buckley et al. 1998) and from the preliminary analysis of *CGRO* OSSE observations presented by Sturner et al. (1997). We tried different parameter sets to fit the observations.

In Figure 1, νF_ν fits to the observations of IC 443 are presented for the model described in the previous section. The preshock density is taken to be $n = 25$ cm^{-3}, and the assumed distance to IC 443 is 1.5 kpc (e.g., Fesen & Kirshner 1980). Interstellar photoelectric absorption of the X-ray spectrum is accounted for with a line-of-sight column density $N_{\rm H} = 2 \times 10^{21}$ cm^{-2} using the cross sections from Morrison & McCammon (1983).

For $v_{S7} = 1.5$ in the diffusion model described by equation (2), we used $k_{(\rm III)0} = 1.1 \times 10^{20}$ cm^2 s^{-1}, $a = 1.0$, $E(p_*) = 1$ MeV, and $E(p_{**}) = 20$ GeV, which are compatible with theoretical estimates of resonant wave-particle interactions. The corresponding value of $\eta \approx 30$. While in principle η can be determined from observations of heliospheric shocks, single spacecraft observations do not provide direct values and are subject to ambiguous interpretation. Values of $\eta \sim 30$ are consistent with modeling of the highly oblique solar wind termination shock (Ellison et al. 1999), but smaller values ($\eta \sim 3$–10) have been inferred for interplanetary traveling shocks (Baring et al. 1997). On the other hand, very weak scattering ($\eta \sim 100$) has been inferred from observations near corotating interaction regions (e.g., Fisk, Schwadron, & Gloeckler 1997) and in the solar wind when the interplanetary magnetic field is nearly radial (e.g., Möbius et al. 1998). We use $\eta \approx 30$ as a conservative value. If strong MHD turbulence is present in the upstream shock region, the η values could be closer to 1. This might allow an electron acceleration model similar to that described earlier, but for slower shock velocities ($\lesssim 100$ km s^{-1}).

The diffusion propagation model is not unique. We obtained a similar fit to that presented in Figure 1 for a diffusion model with $k_{(\rm III)0} = 10^{20}$ cm^2 s^{-1}, $a = 0.7$, $E(p_*) =$ 1 MeV, and $E(p_{**}) = 20$ GeV. As mentioned in § 2, there is an important uncertainty concerning the lack of a quantitative model for the generation of large-scale MHD turbulence in the postshock cooling layer. The uncertainty affects the hard X-ray spectral calculations. In view of this, we calculated the expected bremsstrahlung emission for two limiting cases covering the range of uncertainties. Curve 1 in Figure 1 corresponds to fully developed Alfvénic large-scale MHD turbulence in the postshock cooling layer ($E_C = 120$ keV). Curve 2 corresponds to the case of a lack of large-scale MHD turbulence ($E_C = 2$ GeV). While the GeV bremsstrahlung emission (as well as synchrotron and inverse Compton emission) is similar in the two cases, the hard X-ray emission is sensitive to the uncertainty. We also obtained a similar fit to that presented in Figure 1 for a model with $v_{S7} = 1.1$ and a diffusion model described by $k_{(\rm III)0} = 5 \times 10^{19}$ cm^2 s^{-1}, $a = 1.0$, $E(p_*) = 1$ MeV, and $E(p_{**}) = 10$ GeV. The model with $v_{S7} \approx 1.1$ requires a somewhat higher power conversion efficiency than that with $v_{S7} \approx 1.5$ (see § 3.6), but this value is preferred for the IC 443 radiative shock velocity (Chevalier 1999).

The model of electron injection from the cloud thermal pool described above is based on the ionization structure of a radiative shock, which is very sensitive to the shock velocity if $v_{S7} \sim 1$ (Shull & McKee 1979; Hollenbach & McKee 1989). In this respect, it is instructive to consider a model in which high-energy electrons are not related to freshly injected particles, but are reaccelerated cosmic-ray electrons (Blandford & Cowie 1982; Chevalier 1999; Cox et al. 1999). To model that case we suppose that the far-upstream electron flux is just that observed for Galactic cosmic-ray electrons near Earth, but extrapolated back to the energy $E_{\rm crm}$ with the same slope as observed above a GeV. The calculations of νF_ν for this case are shown in Figure 2. We consider the radiative shock structure with the parameters described in § 2 (the same as were used for Fig. 1). The Galactic cosmic-ray electron flux in the far-upstream region was taken to be $3 \times 10^{-2}(E/\rm GeV)^{-3} e^{\pm}$ s^{-1} cm^{-2} GeV^{-1} sr^{-1} (e.g., Berezinsky et al. 1990) for $E \geq E_{\rm crm}$. We assumed a flat cosmic-ray electron spectrum below $E_{\rm crm}$, corresponding to flattening resulting from Coulomb losses in the interstellar medium. The maximum energy of cosmic-ray

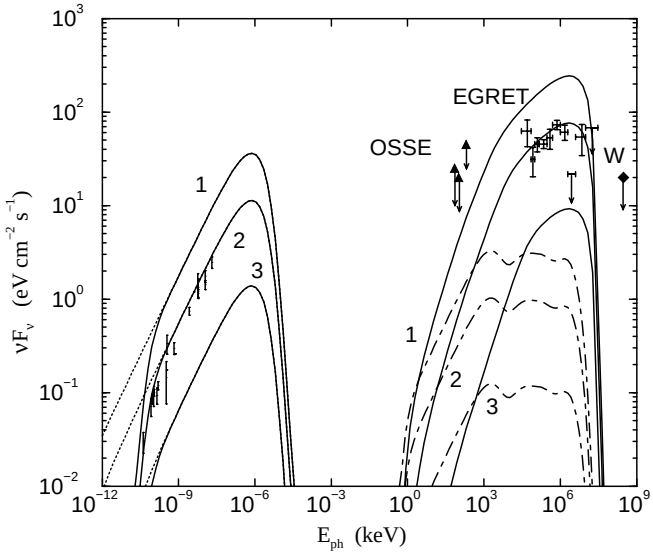

FIG. 2.—Broadband νF_ν spectrum of the shell of IC 443 calculated for the model of Galactic cosmic-ray electron reacceleration by a radiative shock. The basic shock parameters are as in Fig. 1. The low-energy cutoff of the preexisting Galactic cosmic-ray electron spectrum in the cloud is 3 MeV for curve 1, 8 MeV for curve 2, and 50 MeV for curve 3. The inverse Compton emission from the whole remnant is shown as dashed lines.

electrons reaccelerated by the radiative shock is $E_m \sim 10$ GeV (see eq. [3]), as in the case shown in Figure 1. The energy $E_{\rm crm}$ was considered as a free parameter here. We do not distinguish between electrons and positrons because there is no difference between them in the MHD shock acceleration process considered above and most of the emission from high-energy leptons involved in our model remains the same for both kind of particles. Because of interactions with the radiative shock structure, accelerated cosmic-ray electrons could provide a good fit for both synchrotron radio and EGRET emission if $E_{\rm crm} \leq 10$ MeV for the radiative shell parameters described above but fall short for $E_{\rm crm} \approx 100$ MeV.

The relatively low energies, $E_{\rm crm} \sim 10$ MeV, required for the IC 443 shell are a potential problem for this model. The radio synchrotron radiation from the Galaxy indicates that the cosmic-ray electron spectrum flattens to $N(E) \propto E^{-2}$ below energies ~ 1 GeV (Webber 1983). If we use such a spectrum in our model, the nonthermal emission is significantly below that observed. However, there are uncertainties about betatron-type acceleration in the shock compression, about the magnetic field strength, and about the volume of the emitting region. Duin & van der Laan (1975) did successfully model the IC 443 radio flux with a cosmic-ray compression model. We found that models with a higher magnetic field and/or larger volume could reproduce the radio flux, but that the γ-ray fluxes observed by EGRET could not be achieved. Cox et al. (1999) have recently concluded that cosmic-ray compression by radiative shocks could provide a good fit to radio and γ-ray emission from W44 if the cosmic-ray electron population in the vicinity of the SNR is higher than that of measured in solar neighborhood. They used a somewhat higher magnetic field ($B \sim 200$ μG) in the radiative shell of W44 than the 60 μG field we assumed for the IC 443 shell.

The acceleration time is a constraining parameter in our model because of the relatively low shock speed $v_{S7} \sim 1.5$ in the dense medium. The test particle shock acceleration time $t_a(E)$ can be estimated from the equation

$$t_a = \frac{3}{v_{\rm (I)} - v_{\rm (II)}} \int_{p_0}^{p} \left(\frac{k_{\rm (I)}(p)}{v_{\rm (I)}} + \frac{k_{\rm (II)}(p)}{v_{\rm (II)}} \right) \frac{dp}{p}, \qquad (5)$$

where the velocities v_i are measured in the shock rest frame (e.g., Axford 1981). For the radiative shock parameters described above, the acceleration time for $E \gtrsim 10$ GeV is about 3000 yr for $\eta \sim 30$ (note that $t_a \propto \eta$), consistent with the age of IC 443 estimated from the hydrodynamical model by Chevalier (1999). On the basis of *Ginga* observations of IC 443, Wang et al. (1992) suggested an age of about 1000 yr and an association with the supernova of AD 837. The reasons for the low age are related to a thermal interpretation of the observed X-ray emission above 10 keV. We shall argue below for the nonthermal origin of the hard emission in a radiative shock model. A distinctive feature of the radiative shock SNR shell model with direct injection of the electrons from the thermal pool is a hard spectrum of nonthermal emission extending from keV to GeV energies (Fig. 1). There is also a hard-emission component due to inverse Compton emission of relativistic electrons having a scale comparable to the scale of the whole radio image of the remnant.

3.2. *Radio Emission from the Shell*

Observations of the radio emission from IC 443 were performed with different instruments over the last 35 years (see, e.g., Erickson & Mahoney 1985; Green 1986; Claussen et al. 1997 and references therein). The 151 and 1419 MHz radio maps (Green 1986) reveal that the most intense flux comes from the shell of the remnant. We suggest that the eastern part of the shell is a radiative shock which has a high magnetic field and electron flux, dominating the synchrotron radiation from the remnant.

We calculated the synchrotron radiation from the remnant using the local emissivity given by equation (A17). The integrated spectrum from the remnant is dominated by the emission from the radiative shell (having magnetic field $B \sim 6 \times 10^{-5}$ G) if the magnetic field in the central parts of the remnant (region [V]) is moderate, $B \leq 4 \times 10^{-6}$ G. For modeling the shell emission, we took into account the interstellar free-free absorption at low radio frequencies, assuming a column density to IC 443 of $N_{\rm H} \approx 2 \times 10^{21}$ cm^{-2} and an average interstellar medium temperature $T \approx 10^3$ K. This column density is similar to that adopted for the recent analysis of *ASCA* data by Keohane et al. (1997) and is about 4 times less than the value used earlier by Petre et al. (1988) and Wang et al. (1992). We assumed that the ionization fraction is $\sim 15\%$. The free-free absorption inside the cool radiative shell is not very important above 50 MHz because the emission measure is about 1 cm^{-6} pc. The solid and dot-dashed lines in Figure 1 show the total synchrotron radiation from IC 443 (dominated by shell emission in our model) expected at the Earth compared to the observational data (Erickson & Mahoney 1985). Both of our models are illustrated: direct injection of thermal electrons (Fig. 1) and reacceleration of preexisting cosmic-ray electrons by a radiative shock (Fig. 2). A radiative shock with total compression ratio $\delta_t = 4.4$, including a shock precursor and subshock ($\delta_s = 3.3$), was considered. An important feature of the radio observations of IC 443 and W44 is that their spectral indices are relatively flat, implying electron energy spectra flatter than those produced by standard strong shock acceleration in the test particle

limit. In our model, the calculated radio spectrum fits that observed from the IC 443 shell because of the large shock compression ratio $\delta_t \approx 4.4$ and to a lesser extent because of the effect of second-order Fermi acceleration discussed recently by Ostrowski (1999).

3.3. *Nonthermal Emission from a Shocked Clump*

Molecular clouds show complex structure with an ensemble of dense massive clumps embedded in the interclump medium (Blitz 1993). We considered the possibility of radiative shock interaction with dense molecular clumps, resulting in high-energy emission. In IC 443 and W44, those regions do not appear to be significant sites of GHz radio continuum emission, but the clumps may contain most of the cloud mass and are possible sites of hard X-rays and MeV γ-ray emission. The interaction of a radiative shell with a molecular clump generates a dense slab bounded by two shocks (Chevalier 1999). The forward shock propagating into the clump is strong (see also the simulations of Jones & Kang 1993). Since the clump size is typically smaller or comparable to that of the radiative shock layer, it is embedded in a pool of nonthermal particles created by the radiative shock according to the scenario described above. Accelerated particles as well as ionizing radiation from the hot interior regions of the SNR should provide ionization of the external portions of a dense clump at the level $\gtrsim 1\%$. This is sufficient for a shock propagating into the dense clump with $n \sim 10^4$ cm^{-3} and $B \sim 0.1$ mG (e.g., Claussen et al. 1997) to be collisionless. The percent ionization level provides Alfvén Mach numbers $M_A \gtrsim 1$ and weak damping of collisionless Alfvén waves up to wavelengths $\sim 10^{10}$ cm for a flow with velocity $\gtrsim 25$ km s^{-1} in the clump. Then the injection and acceleration processes considered above would be efficient and the ionization in the preshock region would be maintained self-consistently at least at a percent level even for a shock propagating inside the dense clump.

The gas ionization by UV radiation in the radiative shock precursor is sensitive to the shock speed if $v_{S7} \leq 1.1$ (Shull & McKee 1979; Hollenbach & McKee 1989). This implies that a shock having $v_{S7} \leq 1$ propagating in a dense clump would be able to accelerate electrons only below $E_m < 1$ GeV (see eq. [3]). We shall estimate below also the gas ionization rate due to accelerated nonthermal particles. The lifetime of a preexisting electron of MeV energy against ionization losses in the interclump medium ($n \sim 10$ cm^{-3}) is about 10^4 yr. Unless a nearby source of fresh accelerated electrons is present, Galactic cosmic-ray MeV electrons are unlikely to be present in the cloud. Direct injection of electrons from the thermal pool of the weakly ionized precursor would be a dominant source of shock-accelerated electrons up to the cutoff energy E_m. Because of a lack of accelerated GeV electrons in that case ($v_{S7} \leq 1$) the source would not appear as a bright radio and hard EGRET γ-ray emission feature. Nevertheless, these shocks might manifest themselves as hard X-ray and MeV γ-ray emission sources with $\nu F_\nu \propto \nu^a (a \gtrsim 0.5)$ up to a few MeV and with a soft spectrum at higher energies. A comparison of Figure 3 with Figure 1 shows that the hard X-ray flux at 7 keV and above could be dominated by the emission from the shocked clumps, which is consistent with *ASCA* observations of IC 443 presented by Keohane et al. (1997). The hard X-ray nonthermal emission flux may be variable on a timescale of years. A relatively high MeV emissivity is a distinctive feature of shocked clumps, but they are difficult to observe. They must be nearby (within a few hundreds of parsecs) to be detected with COMPTEL/*CGRO* OSSE.

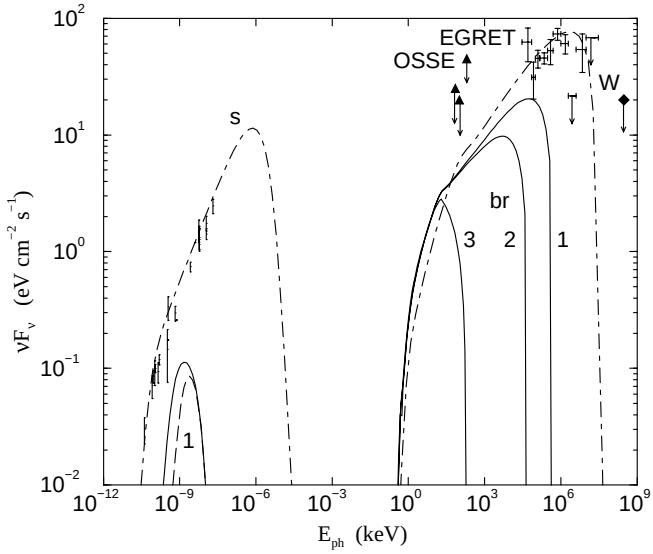

FIG. 3.—Broadband νF_ν spectrum for a model of nonthermal electron production by a radiative shock interacting with a molecular clump (distance 1.5 kpc). The model spectra are calculated for the case of a shock velocity in the clump of 100 km s^{-1}, a number density of 10^3 cm^{-3}, and a magnetic field strength of 2×10^{-4} G. The electron diffusion coefficient (see eq. [2]) $k_{(\mathrm{III})0} = 3 \times 10^{18}$ cm^{-2} s^{-1}, $a = 1.0$, and $E(p_*) = 1$ MeV. The maximum energy of accelerated electrons is $E_m = 0.5$ GeV (*curve 1*) and $E_m = 0.05$ GeV (*curve 2*). The model spectrum for the case of a 30 km s^{-1} shock in a clump with number density 10^4 cm^{-3} is shown by curve 3 (see the text). Interstellar absorption of the radio emission is as in Fig. 1. The internal absorption at the shocked clump is shown for EM ≈ 110 cm^{-6} pc (*solid line radio spectrum*) and EM ≈ 900 cm^{-6} pc (*dashed line radio spectrum*). The dot-dashed curves are the shell emission spectra from Fig. 1 given for comparison.

For a forward shock of velocity $v_{S7} \leq 1$ propagating into a dense clump of number density $n \sim 10^3$ cm^{-3} with upstream ionization level of a few percent [at $\sim k_{(\mathrm{I})}(E_m)/v_S$ distance], the upper cutoff energy $E_m \lesssim 0.5$ GeV. This is about 40 times less than that for a radiative shock in the interclump medium. The spatial diffusion k_{i0} below p_* scales as $w_i \Lambda$. Since the scale of a postshock radiative cooling layer $\propto n^{-1}$ and Λ is a fraction of that, we have $k_{(\mathrm{III})0} \sim 3 \times 10^{18}$ cm^2 s^{-1} in the clump case.

The effective compression of the nonthermal electrons as well as the magnetic field by the system of two shocks bounding the slab could be high. The magnetic field in the clump is expected to be high. Claussen et al. (1997) derived line-of-sight magnetic field strengths of ~ 0.2 mG, remarkably uniform on the scale of several parsecs. Relativistic electrons accelerated by a shock propagating into a clump should produce radio emission with a flat spectrum up to some hundreds of MHz, which is lower than the maximum radio frequency from the shell because of the lower E_m in the clumps. The emission measure of a clump interacting with a radiative shock could be EM $\lesssim 1000$ cm^{-6} pc, which is much higher than that of the shell. Thus, the internal free-free absorption could be important here providing a flatter radio spectrum in the hundreds of MHz regime. This is possibly a reason for the observed spatial variations of the radio spectral index in IC 443 (e.g., Green 1986).

We present in Figure 3 the calculated νF_ν spectrum of nonthermal emission from a radiative shock–molecular

clump interaction region. The forward shock velocity was high, 100 km s^{-1}; the initial number density in the clump was 1000 cm^{-3}; and the shocked clump radius was 0.5 pc. The shock compression ratio was the same as that in the radiative shell model: $\delta_s \approx 3$ and $\delta_t \approx 4.4$. The ionization of gas in the shock upstream was about 5% [at the distances $\sim k_{(I)}(E_m)/v_S$]. To account for some uncertainty in the gas ionization, we present the radio spectra for two possible values of the emission measure EM of the shocked clump: EM = 110 cm^{-6} pc (*solid line*) and EM = 900 cm^{-6} pc (*dashed line*). The diffusion coefficient was $k_{(III)0} \sim 3 \times 10^{18}$ cm^2 s^{-1}, $E(p_*) = 1$ MeV. We illustrate the results for two possible maximal energies of the electrons (depending on the time of shock-clump interaction). Curve 1 in Figure 3 corresponds to $E_m = 0.5$ GeV and $E_m = 0.05$ GeV for curve 2. The synchrotron radio spectrum for curve 2 is below the scale of the plot. The radio spectrum corresponding to curve 1 is very hard because of internal absorption in the shocked clump medium.

We presented above the results for nonthermal emission of a strong radiative shock of $v_{S7} \sim 1$ propagating into a molecular clump. For the case of radiative shock interaction with the molecular clumps in IC 443, lower shock velocities, $v_{S7} \sim 0.3$, are more realistic (e.g., Cesarsky et al. 1999; Chevalier 1999). The preshock ionization may be dominated mostly by nonthermal particles in such a shock because UV radiation is inefficient. A self-consistent model of MHD collisionless shock propagation into a dense clump requires simultaneous simulations of the MHD turbulence spectral properties and the nonthermal particle kinetics. Instead, we suppose that a *collisionless* shock transition exists for $v_{S7} \sim 0.3$ and $n = 10^4$ cm^{-3} and assume the same diffusion model as described in § 2. We calculated the upstream gas ionization, finding that the ionized fraction $x \gtrsim 0.9$ may hold up to depths about 10^{15} cm^{-2} due to shock-accelerated electrons. The Mach number of the shock with $v_{S7} \sim 0.3$ is typically below 5 because of heating of upstream gas up to 10^4 K by accelerated particles, and the compression ratio is lower than 4. The maximum energy of accelerated electrons in that case is typically below an MeV. We illustrate the calculated νF_ν spectrum of nonthermal emission from a 30 km s^{-1} velocity shock ($\delta_t = 3$) interacting with a molecular clump of density 10^4 cm^{-3} by curve 3 in Figure 3; this model corresponds to $k_{(III)0} \sim 7 \times 10^{16}$ cm^2 s^{-1} and $E(p_*) = 10$ keV. Such collisionless shocks, if they exist, would provide a softer spectrum of nonthermal radiation than that for high-velocity shocks with $v_{S7} \gtrsim 1$. A more comprehensive study is required to model the nonthermal emission from the low-velocity shocks in detail. A search for hard X-ray emission correlated with molecular emission predicted by the simplified model described above is possible with high resolution instruments like *Chandra* and *XMM*.

3.4. *Hard X-Ray Emission*

IC 443 was a target of X-ray observations with *HEAO 1* (Petre et al. 1988), *Ginga* (Wang et al. 1992), *ROSAT* (Asaoka & Aschenbach 1994), and *ASCA* (Keohane et al. 1997). *ASCA* gas imaging spectrometer (GIS) observations discovered the localized character of the hard X-ray emission (Keohane et al. 1997). Most of the 2–10 keV GIS photons came from an isolated emitting feature and from the southeast elongated ridge of hard emission. The ridge is also coincident with the 95% confidence error circle of the EGRET *CGRO* source (Esposito et al. 1996), while the isolated feature is outside the circle (Keohane et al. 1997). The integrated 2–10 keV flux observed by *ASCA* GIS was $(5 \pm 1) \times 10^{-11}$ ergs cm^{-2} s^{-1}, representing more than 90% of the total flux from the SNR (Keohane et al. 1997). The hard X-ray ridge, as defined by Keohane et al. (1997), is only a part of the more extended radio shell discussed in the previous section. The flux density at 7 keV from the isolated emitting feature was about 4×10^{-5} photons cm^{-2} s^{-1} keV^{-1} and that from the ridge was 2×10^{-5} photons cm^{-2} s^{-1} keV^{-1}. *HEAO* A-2 measured a flux at 2–10 keV of $(7 \pm 1) \times 10^{-11}$ ergs cm^{-2} s^{-1} (Petre et al. 1988), while *Ginga* measured a 2–20 keV flux of about 9×10^{-11} ergs cm^{-2} s^{-1} (Wang et al. 1992). These numbers are consistent with the assumption that the integrated flux is dominated by the extended soft component coming from the central parts of the remnant.

The soft X-ray 0.2–3.1 keV surface brightness map of IC 443 from the *Einstein Observatory* (Petre et al. 1988) shows bright features in the northeastern part of the remnant. The presence of nearly uniform X-ray emission from the central part of the remnant is a characteristic feature of mixed-morphology SNRs (Rho & Petre 1998). It might be due to the effect of thermal conduction (Cox et al. 1999; Shelton et al. 1999), although Harrus et al. (1997) argued for an alternative radiative shock model for W44, another mixed-morphology SNR. That feature in our model corresponds to the emission from hot ($T \lesssim 10^7$ K), low-density gas interior to the shock (region [V]).

In the radiative shock model with direct injection from the thermal pool and second-order Fermi acceleration in the postshock cooling layer, most of the hard X-ray emission ($\gtrsim 7$ keV) comes from the shell–radiative shock structure with a rising νF_ν X-ray spectrum (curve 1 in Fig. 1 for the shell and curves 1 and 2 in Fig. 3 for a shocked molecular clump). In addition to the shell, there is a more extended source of hard X-rays from inverse Compton emission. It is the dominant source of hard X-rays in the scenario with cosmic-ray electron reacceleration (Fig. 2) and in the case of a lack of second-order Fermi acceleration in the radiative shell (see curve 2 in Fig. 1). In the scenario with reacceleration of cosmic-ray electrons, it is impossible to obtain the 7 keV flux observed by *ASCA* from the IC 443 ridge. Thus, a resolved hard X-ray image of the IC 443 remnant may be very informative in determining the electron acceleration scenario.

The isolated emitting feature in the southern part of IC 443 detected by *ASCA* and brightest around 7 keV has a flat spectrum low-frequency radio continuum source (Green 1986) and is close to a region of excess H_2 emission. High spatial resolution observations of this isolated emitting feature are required to decide between a low-luminosity pulsar nebula and shock interaction models (e.g., radiative shock interaction with a dense molecular clump, Fig. 3). Observations of the hard emission with the sensitivity and resolution available with *BeppoSAX*, *Chandra XRO*, *XMM*, and *Gamma-Ray Large Area Space Telescope* (*GLAST*) would be required to constrain the extension and spectral properties of the hard X-ray emission from IC 443.

3.5. *Gas Ionization by Nonthermal Electrons*

Nonthermal particles accelerated by an MHD collisionless shock wave provide an efficient ionizing agent. We calculated above the nonthermal emission generated by

accelerated energetic electrons; one can also calculate the ionization produced by the same electrons in the molecular cloud. This might connect the high-energy observations with radio, IR, and optical emission from shocked atomic and molecular gas. To estimate the gas ionization due to accelerated electrons in the radiative shock structure, we used the electron spectra calculated with the kinetic model of electron acceleration and propagation described in § 2 and electron ionization cross sections from Appendix B. In Figure 4, we present the calculated ionization rate ζ_e and estimated ionized fraction x in the shell of a radiative shock due to accelerated electrons for the case of $v_{S7} = 1.5$ for both models of large-scale turbulence in the postshock cooling layer considered in § 3.1. There should also be contributions to x from accelerated nucleons and from UV radiation which are not included in Figure 4. We accounted for only radiative recombination, assuming a small molecular fraction in the radiative shell at column densities below 2×10^{20} cm^{-2}.

The solid curves in both panels of Figure 4 correspond to the case of fully developed Alfvénic turbulence in the postshock cooling layer, which provides efficient second-order Fermi acceleration making Coulomb losses relatively unimportant above $E_C = 120$ keV. This case corresponds to curve 1 in Figure 1 for emission from the shell with substantial hard X-ray emission. The dotted lines in Figure 4 correspond to the case of a lack of large-scale MHD turbulence where the Coulomb losses overcome the second-order Fermi acceleration up to $E_C = 2$ GeV. The nonthermal emission expected in this case is illustrated by curve 2 in Figure 1. The radiative shell ionization by nonthermal electrons is sensitive to the turbulent structure of the postshock cooling layer, and there is a correlation between the hard X-ray spectrum and the ionization structure of the radiative shell. We shall consider the effect of nonthermal particles on the ionization structure of a shocked clump elsewhere.

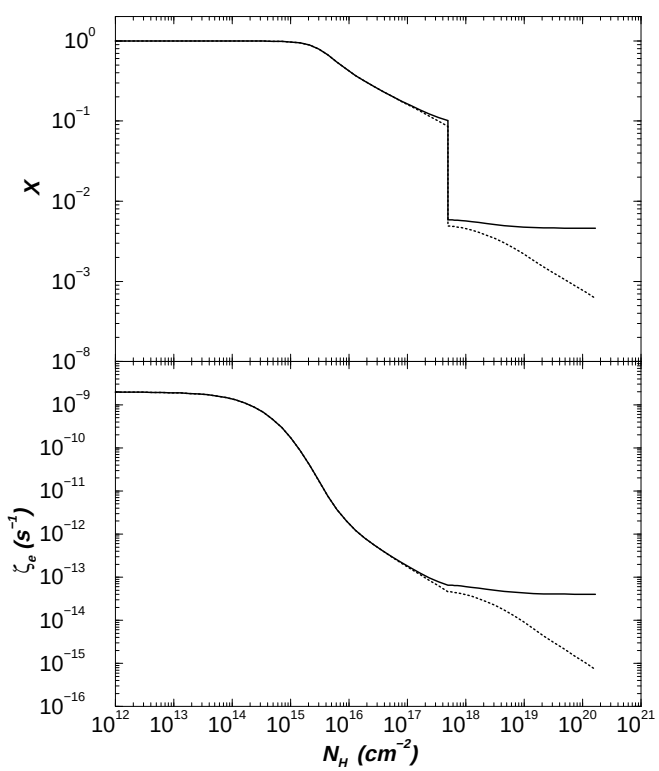

FIG. 4.—Postshock ionization rate due to nonthermal electrons ζ_e (*lower panel*) and the estimated ionization fraction x (*upper panel*) vs. total H column density. The solid lines correspond to the model with $E_C = 120$ keV (see Fig. 1, *curve 1*) and the dotted lines to $E_C = 2$ GeV (see Fig. 1, *curve 2*).

3.6. *Energy in Nonthermal Electrons*

The energy of the electron component for the parameter set used to compute the spectra in Figure 1 is substantial. The power required for electron acceleration and maintenance for curve 1 in Figure 1, $\sim 1.5 \times 10^{37}$ ergs s^{-1}, is high because of the strong Coulomb losses of keV electrons in the dense ionized medium, but it is consistent with the estimate of the total radiative losses from IC 443, dominated by infrared emission (Mufson et al. 1986; Burton et al. 1990). A similar power is required for both models 1 and 2 in Figure 3, where radiative shock–molecular clump interaction is illustrated. For curve 2, the power requirements are less, $\sim 6 \times 10^{36}$ ergs s^{-1}. The implied efficiency of power conversion from the MHD shock flow (which can be estimated as 3×10^{38} ergs s^{-1}) to the nonthermal electrons is about 5% in these cases. The model with $v_{S7} \approx 1$ would provide emission similar to that shown in Figure 1, but requires about 3 times higher efficiency. This is higher than the electron acceleration efficiency estimated from GeV regime cosmic rays observed near the Earth, but evolved SNRs interacting with dense molecular gas probably cannot be considered as the main source of the observed Galactic cosmic rays because of the relatively low maximum energies of accelerated particles.

The pressure of the nonthermal electron component downstream of the shock (region [IV]) is $\mathscr{P}_e \approx 7 \times 10^{-11}$ ergs cm^{-3}. The magnetic pressure in the dense shell is about 1.5×10^{-10} ergs cm^{-3}, which is higher than the thermal gas pressure. The uniform (~ 60 μG) and stochastic magnetic field components dominate the total pressure in the shell.

Let us consider the energy requirements for the scenario with electron injection from preexisting cosmic rays (Fig. 2). The nonthermal electron pressure in this case is $\mathscr{P}_e \approx 5.2 \times 10^{-11}$ ergs cm^{-3} (for $E_{\rm crm} \leq 8$ MeV), similar to that for the model with injection from the thermal pool because it is dominated by GeV particles. An advantage of this scenario is that much less power is required. It is about 4×10^{35} ergs s^{-1}, which is less than 10% of that for the scenario with injection from the thermal pool. The difference is because Coulomb losses are unimportant for the high-energy electrons involved in that scenario. However, a potential problem is the relatively low $E_{\rm crm}$ required. The lifetime of a 20 MeV electron against ionization losses in a neutral medium of number density ~ 1 cm^{-3} is about 10^6 yr. This implies that the source of MeV cosmic-ray electrons should exist within about 100 pc of the molecular cloud if the diffusion coefficient is $\sim 3 \times 10^{26}$ cm^2 s^{-1} at these energies.

4. DISCUSSION AND FUTURE PROSPECTS

For individual SNRs, the ambient density is an important parameter that can be estimated from multiwavelength observations (Chevalier 1999). Another important parameter for modeling the nonthermal particles in an SNR in a molecular cloud is the collisionless MHD turbulence spectrum, particularly in the radiative shock cooling layer. A substantial level of MHD collisionless turbulence could overcome Coulomb losses in the dense plasma downstream

from the radiative shock. An accurate model of MHD turbulence in the postshock cooling layer is not available now. Thus, we considered both limiting cases described in § 2 and show in Figure 1 the uncertainty introduced by the lack of data concerning the MHD turbulence properties. Coulomb losses are important in the postshock cooling region only for electrons with energies below $E_C \approx 20$ keV if the large-scale turbulent velocity has a substantial longitudinal component of ~ 20 km s^{-1}. A higher value ($E_C \gtrsim 8$ MeV) is expected in the absence of a longitudinal component of large-scale turbulence in the postshock cooling layer because the Coulomb losses are overcome by resonant interaction with Alfvén waves. Since the Alfvén velocity is relatively low (~ 5 km s^{-1}), the value of E_C is much higher in that case. We used a conservative minimum value of $E_C = 120$ keV for the radiative shock structure described above, although one could expect $E_C \sim 20$ keV in the most favorable case. The nonthermal emission of SNRs in a molecular cloud (especially in the hard X-ray regime) and ionization structure of the radiative shock are sensitive to the MHD turbulence model. Spatially resolved observations of the nonthermal emission from SNRs may be able to constrain models of MHD turbulence.

All of the SNR candidates from the EGRET list—IC 443, γ Cyg, W44, and Monoceros (Esposito et al. 1996)—are old remnants interacting with molecular clouds. The γ-ray emission from electrons accelerated by the radiative shock calculated for the IC 443 parameters presented in Figures 1 and 2 is in good agreement with that observed by EGRET (Esposito et al. 1996) as well as with the upper limits established by Whipple (Buckley et al. 1998). The high-energy γ-rays ($\gtrsim 50$ MeV) from the radiative shell should be spatially correlated with the radio emission. The EGRET telescope detected an extended excess (95% confidence circle $\sim 42'$ in radius) from the Monoceros SNR correlated with the 1.42 GHz radio emission (Esposito et al. 1996). This is in accordance with the model of a leptonic origin of GeV emission from extended SNRs interacting with clouds (de Jager & Mastichiadis 1997). *GLAST* will be an excellent instrument for future γ-ray observations because it will have the capability of spatially resolving the γ-ray emission from SNRs.

Spatially resolved observations of W44, IC 443, 3C 391, and some other mixed-morphology SNRs from the list given by Rho & Petre (1998) with *BeppoSAX*, *Chandra XRO*, and *XMM* would be very valuable tools to test our model. The hard X-ray detector aboard the forthcoming *Astro-E* mission could be used for observations of the hard 10–700 keV continuum with a field of view of $0\overset{\circ}{.}8$ FWHM at 60 keV and $2\overset{\circ}{.}8$ at 500 keV from the extended hard X-ray emission from IC 443, W44, and the Monoceros SNR predicted by the radiative shock model (see Figs. 1 and 3). Spatially resolved spectra are needed to distinguish the shell emission from the shocked clump emission.

Molecular clumps interacting with moderately fast radiative shocks are also expected to be sources of hard X-rays and MeV γ-rays (up to hundreds of MeV). Nonthermal continuum radio emission (hundreds of MHz) with a sharply rising νF_ν spectrum (Fig. 3) and a time-dependent cutoff frequency is expected in the fast-shock model. As a result of potentially substantial internal free-free absorption, the spectrum of radio emission from a localized clump might constrain the ionized gas density in the clump. The MeV γ-ray spectrum of a localized clump may be resolved with the forthcoming γ-ray missions *International Gamma-Ray Astrophysical Laboratory* (*INTEGRAL*) (e.g., Schönfelder 1999; Winkler 1999) and *GLAST*. With an expected angular resolution about $12'$ FWHM, imager IBIS aboard *INTEGRAL* would allow detection of hard X-ray ($\gtrsim 50$ keV) emission from molecular clouds within ~ 1 kpc. A comparison of hard-emission spectra with the radio spectrum can provide valuable information about the density and magnetic field in a clump. A possible variability on a timescale of a few years for clump hard emission and radio emission (on a longer timescale) could further constrain the model.

For low-velocity (below ~ 30 km s^{-1}) shocks interacting with a dense ($\sim 10^4$ cm^{-3}), magnetized ($B \lesssim 0.5$ mG) molecular clump, one may expect hard X-ray emission below the MeV regime correlated with the regions of molecular emission of shocked gas. Nonthermal radio continuum is not expected in the case of low-velocity shocks because of a lack of accelerated relativistic electrons at sufficiently high energies.

Finally, we note that the high density of energetic particles in the vicinity of a shock wave in a molecular cloud can affect the ionization and thermal properties of the gas. Rich molecular spectra have been observed from IC 443 and 3C 391 (Reach & Rho 1999). It will be interesting to see whether there is a signature of the presence of nonthermal particles that can be discerned from the molecular spectra.

A. M. B thanks Hans Bloemen for useful discussions. We are grateful to M. G. Baring for comments and for making available the corrections to the *e-e* bremsstrahlung formulae and to the referee for very constructive comments. The work of A. M. B. and Yu. A. U. was supported by the INTAS grant 96-0390 and that of R. A. C. by NASA grant NAG 5-8232.

APPENDIX A

RADIATIVE PROCESSES

Given the electron distribution function, the high-energy emission flux $J(E_\gamma)$ at a distance R from the source can be calculated from the equation

$$J(E_\gamma) = \frac{1}{4\pi R^2} \int_V dV \, \frac{dn_\gamma(E_\gamma, \boldsymbol{r})}{dt} , \tag{A1}$$

where $dn_\gamma(E_\gamma, \boldsymbol{r})/dt$ is the emissivity, which here includes bremsstrahlung, synchrotron radiation, and the inverse Compton effect. We generally assumed a pure hydrogen composition in our calculations.

High-energy particles penetrating through a partially ionized medium produce photons as a result of interactions with atoms, electrons, and ions. We assumed a Maxwellian distribution for the ambient matter and in most cases took the target ambient particles to be at rest. Then, the emissivity can be calculated from

$$\frac{dn_\gamma(E_\gamma)}{dt} = 4\pi\left(\int_{E_\gamma}^{\infty} dE_e N_p \sigma_{ep}(E_\gamma, E_e)J(E_e) + \int_{E_{\min}}^{\infty} dE_e N_e \sigma_{ee}(E_\gamma, E_e)J(E_e)\right), \tag{A2}$$

where $J(E_e)$ is the electron flux measured in units $\mathrm{s}^{-1}\ \mathrm{cm}^{-2}\ \mathrm{keV}^{-1}\ \mathrm{sr}^{-1}$, σ_{ep} and σ_{ee} are differential cross sections of one photon emission due to electron-proton and electron-electron interactions integrated over angles, and $E_{\min}$ is the minimum energy of incoming electron that could generate a photon with energy E_γ. For *e-p* interactions, $E_{\min} = E_\gamma$ is a good approximation. The correction due to finite proton mass is less than the uncertainty in the cross section. In the case of *e-e* interactions, we used the following equation for $E_{\min}$:

$$E_\gamma = E_{\min} m_e c^2/[2m_e c^2 + E_{\min} - \sqrt{E_{\min}(E_{\min} + 2m_e c^2)}]\ .$$

The inverse bremsstrahlung contribution is negligible unless there is a very high (far in excess of 100) ratio of protons to electrons.

We used the following cross section approximations in our calculations.

A1. *e-e* BREMSSTRAHLUNG

Haug (1975) has obtained a general formula for the *e-e* bremsstrahlung cross section, but it is more convenient to use simplified approximations. We used relativistic and nonrelativistic asymptotic expressions, which were matched in the intermediate-energy region (see Baring et al. 1999).

In the relativistic limit, we used approximate formulae given by Baier, Fadin, & Khoze (1967) with a correction factor from Baring et al. (1999)[1]:

$$\sigma_{ee}(E_e, E_\gamma) = (\sigma_1 + \sigma_2)A(\epsilon_\gamma, \gamma_e)\ , \tag{A3}$$

where $\gamma_e = (E_e + m_e c^2)/m_e c^2$, $\epsilon_\gamma = E_\gamma/m_e c^2$,

$$\sigma_1(\gamma_e, \epsilon_\gamma) = \frac{4r_o^2\alpha}{\epsilon_\gamma}\left[1 + \left(\frac{1}{3} - \frac{\epsilon_\gamma}{\gamma_e - 1}\right)\left(1 - \frac{\epsilon_\gamma}{\gamma_e - 1}\right)\right]\left\{\ln\left[2(\gamma_e - 1)\frac{\gamma_e - 1 - \epsilon_\gamma}{\epsilon_\gamma}\right] - \frac{1}{2}\right\}, \tag{A4}$$

$$\sigma_2 = \frac{r_0^2\alpha}{3\epsilon_\gamma}\begin{cases}\left[16(1 - \epsilon_\gamma + \epsilon_\gamma^2)\ln\left(\frac{\gamma_e}{\epsilon_\gamma}\right) - \frac{1}{\epsilon_\gamma^2} + \frac{3}{\epsilon_\gamma} - 4 + 4\epsilon_\gamma - 8\epsilon_\gamma^2\right. & \\ \left. -2(1 - 2\epsilon_\gamma)\ln(1 - 2\epsilon_\gamma)\left(\frac{1}{4\epsilon_\gamma^3} - \frac{1}{2\epsilon_\gamma^2} + \frac{3}{\epsilon_\gamma} - 2 + 4\epsilon_\gamma\right)\right], & \epsilon_\gamma \le \frac{1}{2} \\ \frac{2}{\epsilon_\gamma}\left[\left(4 - \frac{1}{\epsilon_\gamma} + \frac{1}{4\epsilon_\gamma^2}\right)\ln(2\gamma_e) - 2 + \frac{2}{\epsilon_\gamma} - \frac{5}{8\epsilon_\gamma^2}\right], & \epsilon_\gamma > \frac{1}{2}\ ,\end{cases} \tag{A5}$$

$r_0 = e^2/m_e c^2$ is the classical electron radius, $\alpha = e^2/\hbar c$, and

$$A(\epsilon_\gamma, \gamma_e) = 1 - \frac{10}{3}\frac{(\gamma_e - 1)^{1/5}}{\gamma_e + 1}\left(\frac{\epsilon_\gamma}{\gamma_e}\right)^{1/3}\ . \tag{A6}$$

According to Baring et al. (1999), these formulae agree with those from Haug (1975) with an accuracy $\sim 10\%$ for electrons of energy $\gtrsim 5$ MeV.

In the nonrelativistic limit, we used equations from Garibyan (1952) and Fedyushin (1952) with correction coefficients from Baring et al. (1999):

$$\sigma_{ee} = \frac{4r_0^2\alpha}{15\epsilon_\gamma}F\left(\frac{4\epsilon_\gamma}{\gamma_e^2 - 1}\right), \tag{A7}$$

where the photon energy is in the range $0 < \epsilon_\gamma < \frac{1}{4}(\gamma_e^2 - 1)$ and $F(x)(0 < x < 1)$ has the form

$$F(x) = B(\gamma_e)\left[17 - \frac{3x^2}{(2 - x)^2} - C(\gamma_e, x)\right]\sqrt{1 - x} + \left[12(2 - x) - \frac{7x^2}{2 - x} - \frac{3x^4}{(2 - x)^3}\right]\ln\left(\frac{1 + \sqrt{1 - x}}{\sqrt{x}}\right). \tag{A8}$$

The correction coefficients are

$$B(\gamma_e) = 1 + \frac{1}{2}(\gamma_e^2 - 1)\ , \qquad C(\gamma_e, x) = \frac{10x\gamma_e\beta_e(2 + \gamma_e\beta_e)}{1 + x^2(\gamma_e^2 - 1)}\ . \tag{A9}$$

Baring et al. (1999) found less than a 10% difference between equation (A7) and the expressions of Haug (1975) for electron energies $E_e \lesssim 500$ keV.

[1] Equations (A4) and (A6) are somewhat different from that given by Baring et al. (1999). M. G. Baring (1999, private communication) made available the corrections to their original formulae.

A2. *e-p* BREMSSTRAHLUNG

In the nonrelativistic limit, we took the *e-p* bremsstrahlung cross section from Akhiezer & Berestetsky (1957):

$$\sigma_{ep} = \frac{16 r_0^2 Z^2 \alpha m_e^2 c^2}{3 p_1^2} \frac{4\pi^2 \zeta_1 \zeta_2}{(e^{2\pi\zeta_1} - 1)(1 - e^{-2\pi\zeta_2})} \frac{1}{\epsilon_\gamma} \ln\left(\frac{p_1 + p_2}{p_1 - p_2}\right), \tag{A10}$$

which is valid if $\zeta_1 \ll 1$; here $\zeta_i = \alpha Z/\beta_i$.

For the relativistic limit, we used Born approximation formulae from Akhiezer & Berestetsky (1957):

$$\sigma_{ep} = r_0^2 Z^2 \alpha \frac{p_2}{p_1} \left\{ \frac{4}{3} - 2\epsilon_1 \epsilon_2 \frac{p_1^2 + p_2^2}{p_1^2 p_2^2} + m_e^2 \left(\frac{\eta_1 \epsilon_2}{p_1^3} + \frac{\eta_2 \epsilon_1}{p_2^3} - \frac{\eta_1 \eta_2}{p_1 p_2} \right) \right.$$
$$\left. + L \left[\frac{8}{3} \frac{\epsilon_1 \epsilon_2}{p_1 p_2} + \frac{\epsilon_\gamma^2}{p_1^3 p_2^3} (\epsilon_1^2 \epsilon_2^2 + p_1^2 p_2^2) + \frac{m_e^2 \epsilon_\gamma}{2 p_1 p_2} \left(\eta_1 \frac{\epsilon_1 \epsilon_2 + p_1^2}{p_1^3} - \eta_2 \frac{\epsilon_1 \epsilon_2 + p_2^2}{p_2^3} + \frac{2\epsilon_\gamma \epsilon_1 \epsilon_2}{p_1^2 p_2^2} \right) \right] \right\}, \tag{A11}$$

where $L = \ln[(p_1^2 + p_1 p_2 - \epsilon_1 \epsilon_\gamma)/(p_1^2 - p_1 p_2 - \epsilon_1 \epsilon_\gamma)] = 2 \ln[(p_1^2 + p_1 p_2 - m_e^2)/m_e \epsilon_\gamma]$, $\eta_1 = \ln[(\epsilon_1 + p_1)/(\epsilon_1 - p_1)] = 2 \ln[(\epsilon_1 + p_1)/m_e]$, and $\eta_2 = 2 \ln[(\epsilon_2 + p_2)/m_e]$. In the velocity range $Z\alpha(\beta_2^{-1} - \beta_1^{-1})$, we included the Elwert factor from Koch & Motz (1959): $f_E = \{\beta_1[1 - \exp(-2\pi Z\alpha/\beta_1)]\}/\{\beta_2[1 - \exp(-2\pi Z\alpha/\beta_2)]\}$.

In equation (A11), $c = 1$ is assumed. In the intermediate energy range, we matched equation (A10) and equation (A11).

A3. SYNCHROTRON RADIATION

We used standard formulae for synchrotron radiation in our calculations (e.g., Ginzburg 1979). The emissivity can be written as

$$E_\gamma \frac{dn_\gamma(E_\gamma)}{dt} = \frac{\sqrt{3}\alpha e}{m_e c} \int d\chi \, dE N(E, \chi) H \sin^2(\chi) F\left(\frac{\nu}{\nu_c}\right),$$
$$F(x) = x \int_x^\infty K_{5/3}(\eta) d\eta, \tag{A12}$$

where χ is the angle between the electron velocity and the magnetic field, $N(E, \chi)$ is the electron distribution function over energy and angle, $\nu_c = \{[3eH \sin(\chi)/4\pi m_e c](E/m_e c^2)\}^2$, and $K_{5/3}(x)$ is the McDonald function. Integrating equation (A12) over angle under the assumption of a chaotic magnetic field orientation, we obtain the equation

$$E_\gamma \frac{dn_\gamma(E_\gamma, \boldsymbol{r})}{dt} = \frac{\sqrt{3}\alpha e}{2\pi m_e c} \int dE N(E, \boldsymbol{r}) H_\perp F\left(\frac{\nu}{\nu_c}\right), \tag{A13}$$

where $N(E, \boldsymbol{r})$ is the electron distribution function as a function of energy and position and $H_\perp = \sqrt{2/3} H(\boldsymbol{r})$ is the averaged magnetic field.

A4. INVERSE COMPTON EMISSION

High-energy electrons colliding with photons result in high-energy photon production (e.g., Jones 1968; Gaisser et al. 1998; Sturner et al. 1997; Baring et al. 1999). If the electron energy $E_e \ll (m_e^2 c^4/4E_\gamma) \approx (6 \times 10^{10})/E_\gamma(\text{eV})$ eV (E_γ is the energy of the emitted photon), then the formula in the Thompson limit is (e.g., Ginzburg 1979)

$$\frac{dn_\gamma(E_\gamma)}{dt} = \sqrt{3}\pi\sigma_T m_e c^2 \int dE_{ph} \sqrt{\frac{E_\gamma}{E_{ph}}} N_{ph}(E_{ph}, \boldsymbol{R}) J_e\left(m_e c^2 \sqrt{\frac{3E_\gamma}{4E_{ph}}}, \boldsymbol{R}\right), \tag{A14}$$

where $\sigma_T = (8\pi/3)(e^2/m_e c^2)^2$ is the Thompson cross section, $N_{ph}(E_{ph})$ is the background photon energy spectrum, and $J_e(E)$ is the incoming electron flux.

If the electron energy $E \geq (m_e^2 c^4/4E_\gamma) \approx (6 \times 10^{10})/E_\gamma(\text{eV})$ eV, we must use the Klein-Nishina formulae (integrated over angles):

$$\frac{dn_\gamma(E_\gamma)}{dt} = 4\pi \int dE_e \, dE_{ph} \, N_{ph}(E_{ph}) \sigma_{KN}(E_\gamma, E_e, E_{ph}) J(E_e), \tag{A15}$$

$$\sigma_{KN}(E_\gamma, E_e, E_{ph}) = \frac{2\pi r_0^2}{\epsilon_{ph} \gamma_e^2} \left[2q \ln(q) + 1 + q - 2q^2 + \frac{q^2(1-q)\Gamma^2}{2(1+q\Gamma)} \right], \tag{A16}$$

where

$$\Gamma = 4\epsilon_{ph} \gamma_e, \qquad q = \frac{\epsilon_\gamma}{(\gamma_e - \epsilon_\gamma)\Gamma}, \qquad 0 \leq q \leq 1.$$

In the above, $\epsilon_\gamma = E_\gamma/m_e c^2$, $\epsilon_{ph} = E_{ph}/m_e c^2$, γ_e is the electron Lorentz factor, and $r_0 = e^2/m_e c^2$ is the classical electron radius. The interstellar background photon spectrum, $N_{ph}(E_{ph}, R)$, was adopted from Mezger et al. (1982) and Mathis, Mezger, & Panagia (1983) taking into account infrared data from Saken, Fesen, & Shull (1992) for the case of IC 443 (see also Gaisser et al. 1998).

A5. FREE-FREE ABSORPTION

Radio waves propagating in the partially ionized thermal plasma are subject to thermal free-free absorption. For $h\nu \ll kT$ (the Rayleigh-Jeans regime), the free-free absorption coefficient α_ν^{ff} (cm^{-1}) can be calculated from

$$\alpha_\nu^{ff} = \frac{4e^6}{3m_e kc}\left(\frac{2\pi}{3km_e}\right)^{1/2} T^{-3/2} Z^2 n_e n_i \nu^{-2} \bar{g}_{ff} \ . \tag{A17}$$

Using an approximate formula for the Gaunt factor $\bar{g}_{ff}(\nu, T)$ from Rybicki & Lightman (1979) appropriate to our parameter range, we obtained a simplified expression for the optical depth $\tau(\nu, T)$:

$$\tau \approx 0.022 \nu_{100}^{-2.1} T_{100}^{-1.34} \mathrm{EM} \ , \tag{A18}$$

where the radio wave frequency ν_{100} is measured in units of 100 MHz, the plasma temperature in units of 100 K is T_{100}, and the emission measure EM is in units of cm^{-6} pc.

APPENDIX B

ELECTRON IONIZATION

The primary ionization rate ζ_e due to electron impact was calculated from the equation

$$\zeta_e = 4\pi \int_{E_{\min}}^{\infty} dE \sigma_{\mathrm{eion}}(E) J_e(E) \ , \tag{B1}$$

where $J_e(E)$ is the electron flux measured in units s^{-1} cm^{-2} keV^{-1} sr^{-1}, σ_{eion} is the differential cross section for hydrogen atom primary ionization by electron-atom interactions integrated over atomic electron states, and $E_{\min}$ is the minimum energy of the ionizing incoming electron.

In the regime below 1 keV, we obtained the following fit to the ionization cross section σ_{eion} using experimental data from Fite & Brackmann (1958):

$$\sigma_{\mathrm{eion}}(E) = \pi a_0^2 A_1 \exp\left(-bA_4 - b^3 A_5 - b^5 A_6\right)/E(\mathrm{eV})^{A_3} \ , \tag{B2}$$

where $b = A_2/E(\mathrm{eV})$ and $E(\mathrm{eV})$ is the incoming electron energy measured in eV. The fitting coefficients are $A_1 = 76.11$, $A_2 = 14.34$, $A_3 = 0.89$, $A_4 = 3.82$, $A_5 = -2.55$, and $A_6 = 4.5$; $a_0 = \hbar^2/m_e e^2$ is the Bohr radius.

At high energies ($\gtrsim 1$ keV), the Born approximation provides good accuracy (e.g., Mott & Massey 1965):

$$\sigma_{\mathrm{eion}} = \int_0^{\kappa_{\max}} \int_{K_{\min}}^{K_{\max}} I_{0\kappa}(K) dK \, d\kappa \ , \tag{B3}$$

where

$$I_{0\kappa}(K) = \frac{2\pi 2^{10}\kappa}{a_0^2 k^2 K} \frac{\mu^6[K^2 + (\mu^2 + \kappa^2)/3]}{[\mu^4 + 2\mu^2(K^2 + \kappa^2) + (K^2 - \kappa^2)^2]^3} \times \exp\left[-\frac{2\mu}{\kappa} \arctan\left(\frac{2\mu\kappa}{K^2 - \kappa^2 + \mu^2}\right)\right] \frac{1}{1 - \exp(-2\pi\mu/\kappa)} \ , \tag{B4}$$

$\mu = Z/a_0$, $k(E)$ is the incoming electron wave number, k_κ is the outgoing electron wave number, and κ is the emitted atomic electron wave number. In addition, $K = |\boldsymbol{k} - \boldsymbol{k}_\kappa|$, $K_{\max} = k + k_\kappa$, and $K_{\min} = k - k_\kappa$.

We found a convenient approximation providing a reasonably accurate fit (better than 10% above 1 keV and better than 5% above 3 keV) to equations (B3) and (B4):

$$\sigma_{\mathrm{eion}}(E) = \pi a_0^2 P_1 E(\mathrm{eV})^{-P_2} \ , \tag{B5}$$

where $P_1 = 97.72$ and $P_2 = 0.93$.

The gas ionization fraction $x = n_i/(n_i + n_n)$ (we consider here a hydrogen plasma) can be expressed through the ionization rate ζ and recombination rate $\alpha_r(T)$ as

$$x = (s^2/4 + s)^{0.5} - s/2 \ , \tag{B6}$$

where $s = \zeta/(\alpha_r n)$. We used the radiative recombination rates given by Spitzer (1978) and dissociative recombination rates from Schneider et al. (1994).

REFERENCES

Akhiezer, A. I., & Berestetsky, V. B. 1957, Quantum Electrodynamics (Oak Ridge: Tech. Information Service Ext.)
Asaoka, I., & Aschenbach, B. 1994, A&A, 284, 573
Asvarov, A. I., Guseinov, O. H., Kasumov, F. K., & Dogiel, V. A. 1990, A&A, 229, 196
Axford, W. I. 1981, in Proc. 17th Int. Cosmic-Ray Conf. (Paris), 12, 155
Baier, V. N., Fadin, V. S., & Khoze, V. A. 1967, Sov. Phys.-JETP, 24, 760
Baring, M. G., Ellison, D. C., Reynolds, S. P., Grenier, I. A., & Goret, P. 1999, ApJ, 513, 311
Baring, M. G., Ogilvie, K. W., Ellison, D. C., & Forsyth, R. J. 1997, ApJ, 476, 889
Berezhko, E. G., & Ellison, D. C. 1999, ApJ, 526, 385

Berezinsky, V. S., Bulanov, S. V., Dogiel, V. A., Ginzburg, V. L., & Ptuskin, V. S. 1990, Astrophysics of Cosmic Rays (Amsterdam: North Holland)
Bertschinger, E. 1986, ApJ, 304, 154
Blandford, R., & Eichler, D. 1987, Physics Rep., 154, 2
Blandford, R. D., & Cowie, L. L. 1982, ApJ, 260, 625
Blitz, L. 1993, in Protostars and Planets III, ed. E. H. Levy & J. I. Lunine (Tucson: Univ. Arizona), 125
Blondin, J. M., Wright, E. B., Borkowski, K. J., & Reynolds, S. P. 1998, ApJ, 500, 342
Boulares, A., & Cox, D. P. 1988, ApJ, 333, 198
Buckley, J. H., et al. 1998, A&A, 329, 639
Burton, M. G., Hollenbach, D. J., Haas, M. R., & Erickson, E. F. 1990, ApJ, 355, 197
Bykov, A. M., & Toptygin, I. N. 1993, Phys. Uspekhi, 36, 1020
Bykov, A. M., & Uvarov, Yu. A. 1999, JETP, 88, 465
Cesarsky, D., Cox, P., Pineau des Forets, G., van Dishoeck, E. F., Boulanger, F., & Wright, C. M. 1999, A&A, 348, 945
Chevalier, R. A. 1977, ApJ, 213, 52
———. 1999, ApJ, 511, 798
Chevalier, R. A., & Imamura, J. N. 1982, ApJ, 261, 543
Claussen, M. J., Frail, D. A., Goss, W. M., & Gaume, R. A. 1997, ApJ, 489, 143
Cox, D. P., Shelton, R. L., Maciejewski, W., Smith, R. K., Plewa, T., Pawl, A., & Rózyczka, M. 1999, ApJ, 524, 179
de Jager, O. C., & Mastichiadis, A. 1997, ApJ, 482, 874
DeNoyer, L. K. 1979, ApJ, 232, L165
Dermer, C. D. 1986, A&A, 157, 223
Draine, B. T., & McKee, C. F. 1993, ARA&A, 31, 373
Drury, L. O'C., Aharonian, F., & Völk, H. 1994, A&A, 287, 959
Drury, L. O'C., Duffy, P., & Kirk, J. G. 1996, A&A, 309, 1002
Duin, R. M., & van der Laan, H. 1975, A&A, 40, 111
Ellison, D. C., Jones, F. C., & Baring, M. G. 1999, ApJ, 512, 403
Erickson, W. C., & Mahoney, M. J. 1985, ApJ, 290, 596
Esposito, J. A., Hunter, S. D., Kanbach, G., & Sreekumar, P. 1996, ApJ, 461, 820
Fedyushin, B. K. 1952, Zh. Eksp. Teor. Fiz., 22, 140
Fesen, R. A., & Kirshner, R. P. 1980, ApJ, 242, 1023
Fisk, L. A., Schwadron, N. A., & Gloeckler, G. 1997, Geophys. Res. Lett., 24, 93
Fite, W. L., & Brackmann, R. T. 1958, Phys. Rev., 112, 1141
Frail, D. A., & Mitchell, G. F. 1998, ApJ, 508, 690
Gaisser, T. K., Protheroe, R. J., & Stanev, T. 1998, ApJ, 492, 219
Garibyan, G. M. 1952, Zh. Eksp. Teor. Fiz., 24, 617
Giacalone, J., Burgess, D., Schwartz, S. J., Ellison, D. C., & Bennett, L. 1997, J. Geophys. Res., 102, 19789
Ginzburg, V. L. 1979, Theoretical Physics and Astrophysics (Oxford: Pergamon)
Green, D. A. 1986, MNRAS, 221, 473
Harrus, I., Hughes, J. P., Singh, K. P., Koyama, K., & Asaoka, I. 1997, ApJ, 488, 781
Haug, E. 1975, Z. Naturforsch., 30a, 1099
Hollenbach, D., & McKee, C. F. 1989, ApJ, 342, 306
Jones, F. C. 1968, Phys. Rev., 167, 1159
Jones, F. C., & Ellison, D. C. 1991, Space Sci. Rev., 58, 259
Jones, T. W., & Kang, H. 1993, ApJ, 402, 560
Keohane, J. W., Petre, R., Gotthelf, E. V., Ozaki, M., & Koyama, K. 1997, ApJ, 484, 350
Koch, H. W., & Motz, J. W. 1959, Rev. Mod. Phys., 31, 920
Koyama, K., Petre, R., Gotthelf, E. V., Hwang, U., Matsuura, M., Ozaki, M., & Holt, S. S. 1995, Nature, 378, 255
Kulsrud, R., & Cesarsky, C. J. 1971, Astrophys. Lett., 8, 189
Levinson, A. 1996, MNRAS, 278, 1018
Mathis, J. S., Mezger, P. G., & Panagia, N. 1983, A&A, 128, 212
McClements, K. G., Dendy, R. O., Bingham, R., Kirk, J. G., & Drury, L. O'C. 1997, MNRAS, 291, 241
Mezger, P. G., Mathis, J. S., & Panagia, N. 1982, A&A, 105, 372
Möbius, E., Rucinski, D., Lee, M. A., & Isenberg, P. A. 1998, J. Geophys. Res, 103, 257
Morrison, R., & McCammon, D. 1983, ApJ, 270, 119
Mott, N. F., & Massey, H. S. W. 1965, The Theory of Atomic Collisions (Oxford: Claredon)
Mufson, S. L., McCollough, M. L., Dickel, J. R., Petre, R., White, R., & Chevalier, R. 1986, AJ, 92, 1349
Ostrowski, M. 1999, A&A, 345, 256
Petre, R., Szymkowiak, A. E., Seward, F. D., & Willingale, R. 1988, ApJ, 335, 215
Reach, W. T., & Rho, J. 1999, ApJ, 511, 836
Reynolds, S. P. 1998, ApJ, 493, 375
Rho, J., & Petre, R. 1998, ApJ, 503, L167
Richter, M. J., Graham, J. R., & Wright, G. S. 1995, ApJ, 454, 277
Rybicki, G. B., & Lightman, A. P. 1979, Radiative Process in Astrophysics (New York: Wiley)
Saken, J. M., Fesen, R. A., & Shull, J. M. 1992, ApJS, 82, 715
Schneider, I. F., Dulieu, O., Giusti-Suzor, A., & Roueff, E. 1994, ApJ, 424, 983
Schönfelder, V. 1999, in LiBeB, Cosmic Rays and Related X- and Gamma-Rays, ed. R. Ramaty, E. Vangioni-Flam, M. Cassé, & K. Olive (San Francisco: ASP), 217
Shelton, R. L., Cox, D. P., Maciejewski, W., Smith, R. K., Plewa, T., Pawl, A., & Rózyczka, M. 1999, ApJ, 524, 192
Shull, J. M., & McKee, C. F. 1979, ApJ, 227, 131
Spitzer, L. 1978, Physical Processes in the Interstellar Medium (New York: Wiley)
Sturner, S. J., Skibo, J. G., Dermer, C. D., & Mattox, J. R. 1997, ApJ, 490, 619
van Dishoeck, E. F., Jansen, D. J., & Phillips, T. G. 1993, A&A, 279, 541
Vishniac, E. T. 1983, ApJ, 274, 152
Völk, H. J., Morfill, G. E., & Forman, M. A. 1981, ApJ, 249, 161
Wang, Z. R., Asaoka, I., Hayakawa, S., & Koyama, K. 1992, PASJ, 44, 303
Webber, W. R. 1983, in Composition and Origin of Cosmic Rays, ed. M. M. Shapiro (Dordrecht: Reidel), 83
Winkler, C. 1999, Astrophys. Lett. Commun., 39, 309